Energy Storage

Mesoporous Tungsten Trioxide Polyaniline Nanocomposite as an Anode Material for High-Performance Lithium-Ion Batteries

Bin Li,[a, b, c] Xiaoping Li,[c] Weishan Li,*[b, c] Yaqiong Wang,[d] Evan Uchaker,[a] Yi Pei,[a] Xi Cao,[a] Shuang Li,[a] Bin Huang,[a] and Guozhong Cao*[a]

Abstract: A nanocomposite of polyaniline (PANI)/mesoporous tungsten trioxide (m-WO$_3$) was synthesized by the chemical oxidation polymerization of aniline coated onto an ordered m-WO$_3$ and investigated as an anode material for lithium-ion batteries. The nanocomposite was characterized by using X-ray diffraction, Fourier transform infrared spectroscopy, thermogravimetric analysis, scanning electron microscopy, and transmission electron microscopy. The electrochemical properties of the nanocomposite were evaluated by cyclic voltammetry and constant current charge/discharge tests. The reversible capacity of the PANI/m-WO$_3$ in the first cycle was 1064 mAh g^{-1} at 60 mA g^{-1} and remained at 803 mAh g^{-1} at 180 mA g^{-1} after 100 cycles, while the initial charge capacity of m-WO$_3$ was 556 mAh g^{-1} and remained only at 303 mAh g^{-1} after 50 cycles. The improved electrochemical performance of the nanocomposite can be ascribed to the electronical conductivity of PANI and the chemical interaction between PANI and m-WO$_3$. More importantly, the unique PANI coating layer on the m-WO$_3$ is believed to play an important role in the capacity contribution of the composite.

Introduction

Lithium ion batteries have been widely used in portable electronics (including mobile phones, laptops, and digital audio players), and are expected to be a promising power source in electric vehicles due to their superior energy density compared to other secondary batteries.[1] To meet the increasing energy density demands in large-scale energy-storage devices, research has been focused on new electrode materials with large capacity density and long cycling stability for the lithium ion battery. Various transition metal oxides, such as Fe$_3$O$_4$,[2]

[a] B. Li, Dr. E. Uchaker, Y. Pei, X. Cao, S. Li, B. Huang, Prof. G. Cao
Department of Materials Science and Engineering
University of Washington
Seattle, Washington 98195 (United States)
E-mail: gzcao@u.washington.edu

[b] B. Li, Prof. W. Li
College of Materials Science and Engineering
South China University of Technology
Guangzhou 510641 (China)
E-mail: liwsh@scnu.edu.cn

[c] B. Li, Prof. X. Li, Prof. W. Li
School of Chemistry and Environment
South China Normal University
Guangzhou 510006 (China)

[d] Y. Wang
Equipe de Chimie Bioorganique et Bioinorganique
Univ Paris-Sud
Bâtiment 420, 91405 Orsay (France)

Fe$_2$O$_3$,[3] Co$_3$O$_4$,[4] SnO$_2$,[5] MoO$_2$,[6] TiO$_2$,[7] and Mn$_2$O$_3$[8] have been proposed as anode materials because of their high capacity or good cycling performance. Among the transition metal oxides, tungsten trioxide (WO$_3$) with a theoretical capacity of 693 mAh g^{-1} offers unique advantages: a very large volumetric capacity density, 5274 mAh cm^{-3}, due to its vast theoretical mass density (7.61 g cm^{-3}), and lower cost.[9] Recently, much effort has been devoted to synthesizing nanostructured WO$_3$ for lithium-ion battery applications, such as nanowires[10] and hollow nanospheres.[11] Mesoporous WO$_3$ (m-WO$_3$) with ordered pore structures has also been investigated and shown to be a good candidate in improving the properties of lithium-ion batteries. For example, Yoon et al.[9] reported that ordered mesoporous tungsten oxide exhibited a high initial reversible capacity of 748 mAh g^{-1} (6.5 Li/W) at 0.1 C and remained at 410 mAh g^{-1} after 30 cycles at 0.2 C, while Liu et al.[12] incorporated mesoporous WO$_3$ with graphene sheets to enhance the mechanical stability during cycling, and the resulting materials also showed a high initial reversible lithium storage capacity of 761 mAh g^{-1} and maintained 617 mAh g^{-1} after the rate performance investigation. However, the large structure and volume variations during the charge/discharge processes lead to a poor cycling stability. It is necessary to further modify this oxide for its practical application in lithium-ion batteries.

Conducting polymers have received much attention in the past decade due to their good electronic conductivity, simple synthesis process, and environmental stability. Recently, a polypyrrole/MoO$_3$ nanocomposite was prepared and exhibited excellent cycling and rate behavior in aqueous rechargeable lithium batteries, demonstrating the successful use of the conduct-

ing polymer in improving electrochemical performance.[13] Polyaniline (PANI) is an another interesting polymer with conductive of 0.5–1.0 S cm^{-1} (HCl doped) and has been used for performance improvement of electrode materials of lithium-ion batteries.[14] Hierarchical hollow spheres of Fe_2O_3@PANI were developed by in situ polymerization of PANI on Fe_2O_3 hollow spheres, and showed higher rate capability and long-term cycling stability compared to the bare Fe_2O_3 spheres.[15] The capacity was improved from 732 mAh g^{-1} for bare hollow Fe_2O_3 to 893 mAh g^{-1} in Fe_2O_3@PANI after 100 cycles. Owing to the good conductivity and high mechanical flexibility of the PANI, silicon nanoparticles (n-Si) were distributed into PANI to buffer the large volume changes of the silicon during the lithiation process, and the n-Si/PANI-graphite composite electrode exhibited ≈ 90 % capacity retention after 130 cycles with capacities around 500 mAh g^{-1}.[16] Hybrid aerogels of carbon nanotubes and PANI nanoribbons were also developed as free-standing, flexible negative electrodes for lithium ion batteries, and demonstrated that the high utilization of PANI could improve the capacity (185 mAh g^{-1}) and cycling performance (no fading up to 200 cycles) of the carbon nanotubes.[17] In our previous study, we showed that the combination of PANI and WO_3 significantly improves the electrochemical activity of platinum-free anodic electrocatalysts in microbial fuel cells in terms of the power density and internal resistance.[18]

In this paper, a mesoporous tungsten trioxide (m-WO_3) composite was synthesized by the use of mesoporous silica KIT-6 as hard template, followed by in situ chemical oxidation polymerization of PANI on the m-WO_3 particles. The mesoporous structure offers large surface area for electrochemical reaction and provides structural flexibility to accommodate the large volume change of WO_3 during charge/discharge, while the conducting polymer coating improves the electrical conductivity and the structural stability. The resultant PANI/m-WO_3 composite was newly evaluated as an anode material for lithium-ion batteries and delivered a high reversible Li-ion storage capacity of 1064 mAh g^{-1} and exhibited good cycling stability. The structural characterization of the resultant composite was performed with X-ray diffraction (XRD), Fourier transform infrared spectrum (FTIR), thermogravimetric analysis (TGA), scanning electron microscopy (SEM), and transmission electron microscopy (TEM), and its performance as an anode for lithium-ion batteries, in terms of high capacity and cycling stability, were evaluated by charge/discharge tests.

Results and Discussion

The formation process of PANI/m-WO_3 composite is illustrated in Figure 1. A hard template of mesoporous silica with cubic Ia3d symmetry (KIT-6) was prepared following a previously reported procedure[19] using triblock copolymer Pluronic P123 ($EO_{20}PO_{70}EO_{20}$) as a template by adding butanol in a 0.5 M hydrochloric acid aqueous solution, and employing tetraethoxysilane (TEOS) as a silica source. The m-WO_3 was synthesized via a replicating route using the mesoporous silica as the template[20] and the PANI/m-WO_3 composite was synthesized via an in situ polymerization process. The obtained template-re-
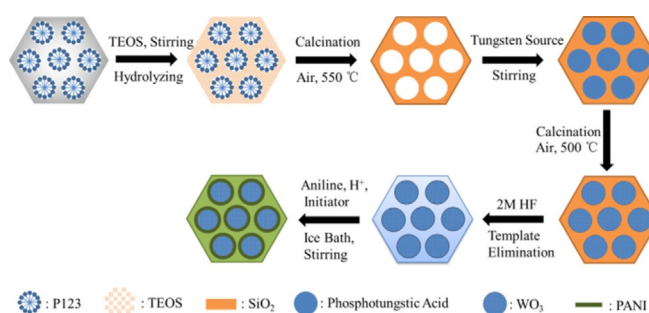

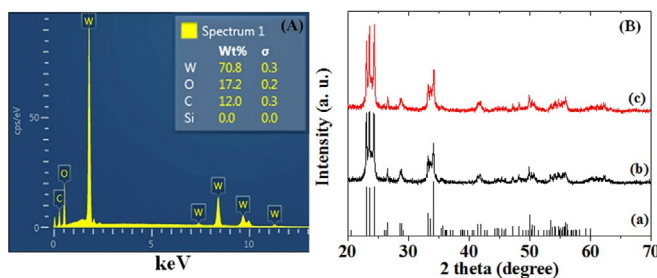**Figure 1.** Schematic diagram for the PANI-coated m-WO_3.

Figure 2. (A) EDS patterns of template-removed WO_3; (B) X-ray diffraction patterns of (a) JCPDS card no. 43-1035, (b) m-WO_3, and (c) PANI/m-WO_3.

moved WO_3 was characterized by EDS and the result is presented in Figure 2(A). The existence of elemental carbon is attributed to the carbon tape under the WO_3 powder sample. Sharp tungsten and oxygen peaks can be observed, while silicon is excluded in the as-prepared sample. This confirms the silica is removed completely after the washing process. Figure 2(B) presents the XRD patterns of the m-WO_3 and PANI/m-WO_3 composites. A well-crystallized WO_3 framework with pure monoclinic WO_3 (JCPDS card no. 43-1035) is observed for both of the samples. It can be noted that there is no significant difference in diffraction patterns between the WO_3 samples, suggesting that the introduction of the PANI coating layer does not disrupt crystallization characteristics of m-WO_3.

The FTIR spectra of the samples are displayed in Figure 3(A). For the sample of PANI (curve a), the absorption bands at 1133 and 1497 cm^{-1} correspond to the stretching vibration of quinoid (N=Q=N), while the peaks at 1570 and 1300 cm^{-1} are attributed to the benzenoid (N—B—N) rings.[21] The peak at around 1249 cm^{-1} can be assigned to the C—N stretching vibration, which is characteristic of proton-doped PANI.[22] As shown in Figure 3(A), PANI/m-WO_3 exhibits characteristic vibrations of PANI, suggesting that the successful synthesis of PANI and the m-WO_3 are dispersed in the PANI matrix. It should be noted that characteristic peaks of N=Q=N shift to 1487 and 1123 cm^{-1}, undergoing around 10 cm^{-1} redshifts. This shift might be ascribed to the interaction between the π-bonded surface of WO_3 and the conjugated structure of quinoid ring in PANI, resulting in a stabilized quinoid ring structure, as shown in Figure 4. In addition, during the chemical polymerization, the nitrogen atoms in benzenold diamine are thought to form coordinated compounds with the exposed tungsten atoms on
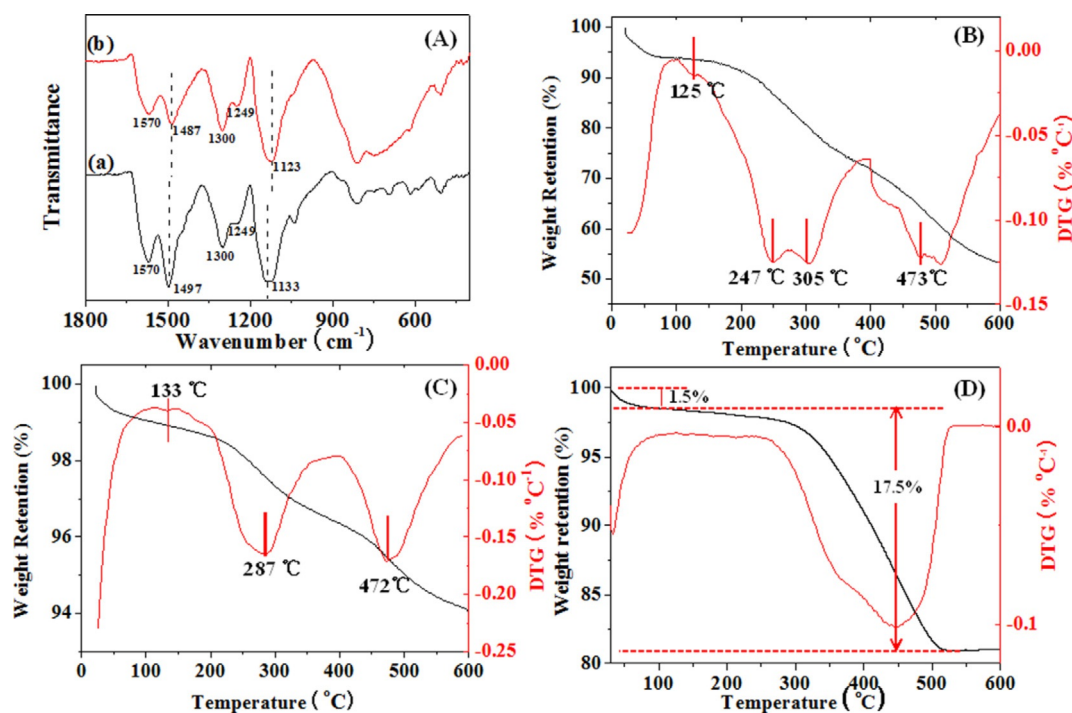
Figure 3. (A) FTIR spectra of (a) PANI, and (b) PANI/m-WO$_3$; TGA curve and DTG curve of PANI (B) and PANI/m-WO$_3$ (C) from 25 °C to 600 °C at a rate of 10 °C min^{-1} in a nitrogen atmosphere; (D) TGA curve and DTG curve of PANI/m-WO$_3$ from 25 °C to 600 °C at a rate of 10 °C min^{-1} in air atmosphere.
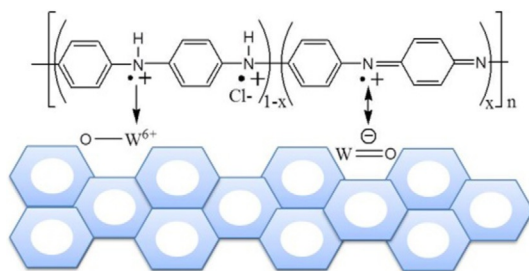
Figure 4. Schematic illustration of possible composite interaction between PANI and WO$_3$ in PANI/m-WO$_3$. x can be varied from 1 to 0 to yield the completely reduced and oxidized forms, respectively.

the surface of WO$_3$.[23] The electron-withdrawing nature of WO$_3$ might be decreased by the delocalization of the lone pair electrons on the nitrogen atoms. This phenomenon likely benefits the migration of Li cations between the electrolyte and the bulk WO$_3$. Therefore, it is expected that the stability and conductivity of PANI/m-WO$_3$ composite can be improved by the chemical interaction between PANI and m-WO$_3$.

The comparison of thermogravimetric analysis for plain PANI and PANI/m-WO$_3$ in the temperature range of 25–600 °C in the nitrogen and air atmosphere can explain the thermal stability and PANI loading in the composite. Figure 3 (B) and Figure 3 (C) show the TGA and DTG curves of PANI and PANI/m-WO$_3$ in a nitrogen atmosphere, respectively. The initial weight loss up to 100 °C is due to the loss of absorbed water molecules in the mesoporous structure. The second weight-loss step between 125 to 200 °C is attributed to the loss of hydrochloric acid dopants.[24] In addition, the endothermic peaks could be generated

by the decomposition of PANI into oligomers and monomers due to chain scission processes of weakly bound aniline molecules. Thus, the third weight-loss range from 200 to 350 °C is mainly due to the evaporation of the monomers from the composite. In the last step, PANI backbone degradation occurs from 400 to 600 °C, which is accompanied by the production of gaseous species.[14c] It can be noted that the overall endothermic peaks positions of the PANI/WO$_3$ in the corresponding DTG curve are higher than that of pure PANI. This suggests that the use of polyaniline in nanocomposite has better thermal stability, which is consistent with other polyaniline-loaded materials[25] and further confirms the FTIR prediction. Figure 3 (D) shows TG/DTG curves of PANI/m-WO$_3$ in air and the PANI content in the composite is 17.5 wt. %.

The SEM and TEM were used to investigate the microstructure formed during the coating process. Figure 5 shows SEM and TEM images of both m-WO$_3$ and the PANI/m-WO$_3$ composite. The m-WO$_3$ particles are honeycomb-like with an average particle size of around 150 nm (Figure 5 (A)), and have a uniform mesoporous structure with the pore size of around 12 nm (Figure 5 (C) and Figure 5 (E)). In the case of PANI/m-WO$_3$, the composite shows some deposits padded onto the surface of the m-WO$_3$ particles (Figure 5 (B)) and the honeycomb-like morphology becomes indistinct (Figure 5 (D)). The high-resolution TEM image in Figure 5 (F) confirms the m-WO$_3$ particles were coated with a ≈ 3 nm thick PANI layer, maintaining the pristine morphology of m-WO$_3$. This result confirms that PANI has been successfully coated on the m-WO$_3$ and does not affect the structure of the m-WO$_3$.

Cyclic voltammograms of m-WO$_3$ and PANI/m-WO$_3$ are shown in Figure 6 (A). A small cathodic current starts from
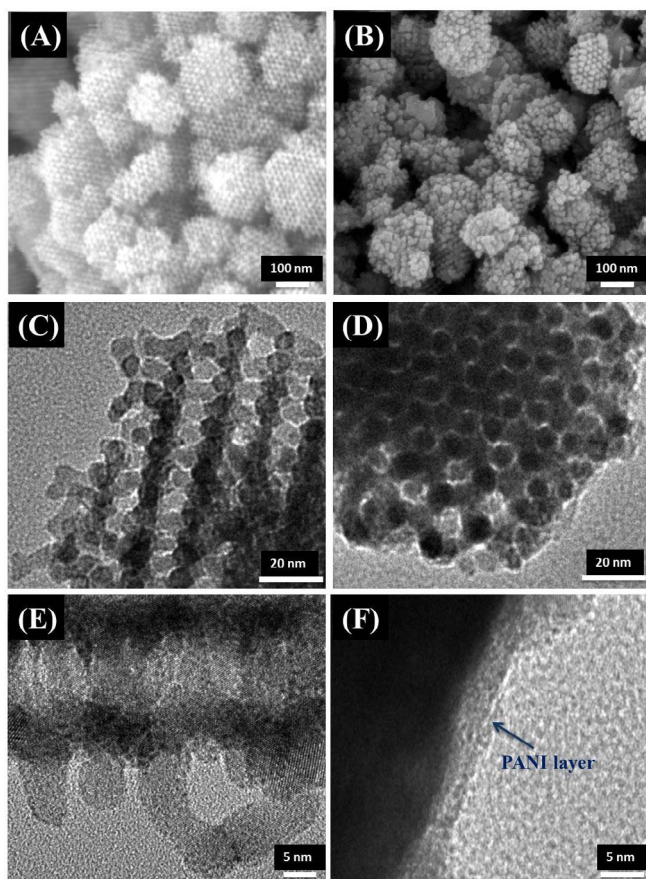
Figure 5. SEM images of (A) template-free m-WO$_3$ and (B) PANI/m-WO$_3$ composite; TEM images of (C, E) m-WO$_3$ and (D, F) PANI/m-WO$_3$ composite, showing that the m-WO$_3$ is uniformly coated with PANI.

2.5 V (vs. Li$^+$/Li), a sharp reduction peak at 0.73 V (vs. Li$^+$/Li) can be identified, and large reduction current at 0.01 V (vs. Li$^+$/Li) is observed in the first discharge process. The corresponding discharging reaction mechanism can be described as follows:[26]
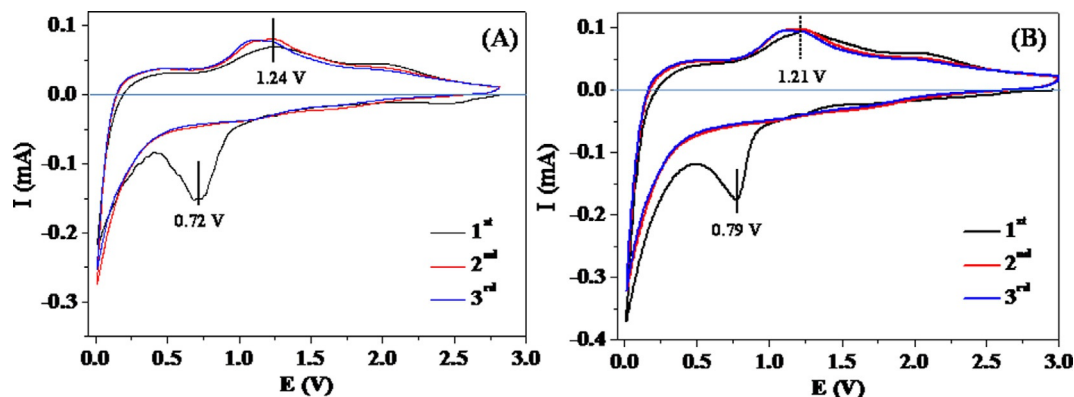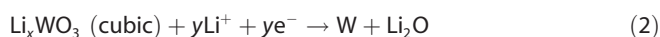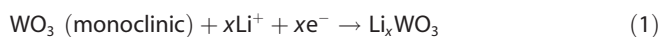
$$WO_3 \ (monoclinic) + xLi^+ + xe^- \rightarrow Li_xWO_3 \quad (1)$$

$$Li_xWO_3 \ (cubic) + yLi^+ + ye^- \rightarrow W + Li_2O \quad (2)$$

The reduction current response and the reduction peak at 0.72 V (vs. Li$^+$/Li) is attributed to the conversion reaction and some irreversible electrochemical process, which may be due to the phase conversion from monoclinic phase ((P21/n) to cubic phase (Pm3m) [Eq. (1)]. The intensity of conversion reaction peak is remarkably decreased in the second cycle but still has reduction current response at around 0.72 V (vs. Li$^+$/Li) when compared to the third cycle. This implies that the monoclinic or the cubic structure disappears in the subsequence cycle but this phase conversion reaction cannot be completed in the initial cycle, which might result in the unstable capacity retention in the first couple of charging/discharging cycles. The large reduction current at 0.01 V (vs. Li$^+$/Li) is corresponding to the complete reduction of W cation to W^0 [Eq. (2)], which is accompanied by the formation of an amorphous-structured product.[26] The broad oxidation peak at about 1.24 V (vs. Li$^+$/Li) during the charge process is ascribed to the oxidation reaction,[27] as shown in Equation (3):

$$W + 3Li_2O \rightarrow zWO_3 + (1-z)W + 6zLi^+ + 3(1-z)Li_2O + 6ze^-$$
$$(3)$$
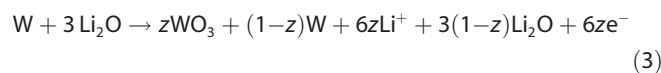
When coated with PANI, the potential of the conversion reaction peak locates at 0.79 V (vs. Li$^+$/Li) and the intensity of this peak is decreased, and the current for lithium insertion is much higher than that of m-WO$_3$, as shown in Figure 6(B). In addition, the oxidation peak potential shifts negatively to 1.21 V (vs. Li$^+$/Li). These results indicate that the coating layer not only improves the electrochemical activity of WO$_3$ but also prevents the irreversible electrochemical process. It can be seen that the shape of the CV profile of tungsten trioxide is similar to that of silicon- or tin-based anodes for lithium ion batteries.[28] Based on the reduction of W cation at the low potential in CV scanning and the shape of the CV curves, it can be considered that the charge and discharge process in WO$_3$ is accompanied by an alloying reaction of Li$_x$W, which might form the BCC alloy system that exists in the tantalum–tungsten system due largely to the similar atomic radius of tantalum and lithium. However, there is neither report in the literature nor direct experimental evidence to support this assumption. Our ex-situ XRD results are simply inconclusive due to the

Figure 6. Cyclic voltammograms of m-WO$_3$ (A) and PANI-coated m-WO$_3$ (B); scan rate: 0.2 mV s^{-1}.

large noise to signal ratio. It is more likely that the first cycle is the conversion-based charging and discharging processes, which might affect the electrochemical performance of the WO_3. Note that larger reduction and oxidation current response was observed in PANI/m-WO_3 composite compared to m-WO_3. The PANI coating layer on the m-WO_3 yields a synergistic effect to promote the reaction at the interface and thus leads to greater cycling capacity than that of m-WO_3.

In order to further demonstrate superior features of PANI/m-WO_3 on electrochemical performance, m-WO_3, PANI-coated m-WO_3 and pure PANI were tested. Figure 7 shows the charge–discharge curves of m-WO_3 and PANI/m-WO_3 at 60 mA g^{-1} for the 1st and 2nd cycle between 0.01–2.5 V (vs. Li$^+$/Li). It can be seen that during the first discharging process the potential of the cells drops from 1.5 V (vs. Li$^+$/Li) to a plateau at around 0.8 V (vs. Li$^+$/Li) and then decreases slowly to 0.01 V (vs. Li$^+$/Li). The former can be ascribed to the conversion reaction and the latter corresponds to the reduction of W^{6+} to W^0, which is consistent with the CV results. The initial charge capacity of m-WO_3 is 556 mAh g^{-1} with a coulombic efficiency of 63.5 %. The large irreversible capacity is likely due to the irreversible electrochemical processes including the formation of the solid electrolyte interphase (SEI) layer and the irreversible WO_3 conversion reaction with lithium. In the case of PANI/m-WO_3, the coulombic efficiency of the composite is 67.2 % and the reversible capacity in the first cycle is 1064 mAh g^{-1} which is much higher than the theoretical capacity (693 mAh g^{-1}). However, the reversible capacity of pure PANI in the first cycle is

30 mAh g^{-1} (Figure 7 (C)), which is comparable with the values reported in literature,[29] and it seems that PANI has little contribution to the capacity of the m-WO_3. Previous research also showed that a higher capacitance was observed in PANI/m-WO_3 electrode used in electrochemical capacitors application compared with m-WO_3.[30] The improvement might be ascribed to the chemical interaction between the polymer matrix and the WO_3 particles, which is beneficial to the migration of Li cations between the electrolyte and the bulk WO_3, resulting in a higher electrochemical performance.

The cycling performance of m-WO_3, PANI/m-WO_3 and plain PANI are displayed in Figure 8 (A). The cells were charged/discharged at a current density of 60 mA g^{-1} for initial two cycles, followed by cycling at a current density of 180 mA g^{-1} in the voltage range of 0.01–2.5 V (vs. Li$^+$/Li). The reversible capacity of the bare PANI electrode is 17 mAh g^{-1} after 100 cycles and shows a high cycling stability, indicating that PANI is stable in the lithium-ion battery system. The cell of m-WO_3 shows a fast reversible capacity decrease, dropping from 449 mAh g^{-1} in the 3rd cycle to 303 mAh g^{-1} after 50 cycles, which is similar to the observations by other research groups.[9, 11] However, when PANI is loaded, the capacity is 883 mAh g^{-1} at the current density of 180 mA g^{-1} and the reversible capacity remains 803 mAh g^{-1} after 100 cycles, exhibiting a better retention property compared to m-WO_3. Such capacity retention was examined further by increasing the charge/discharge current densities. The electrode was tested at 0.18, 0.3, 0.6, 1.8, 3.0, and 6.0 A g^{-1}. As shown in Figure 8 (B), the corresponding re-

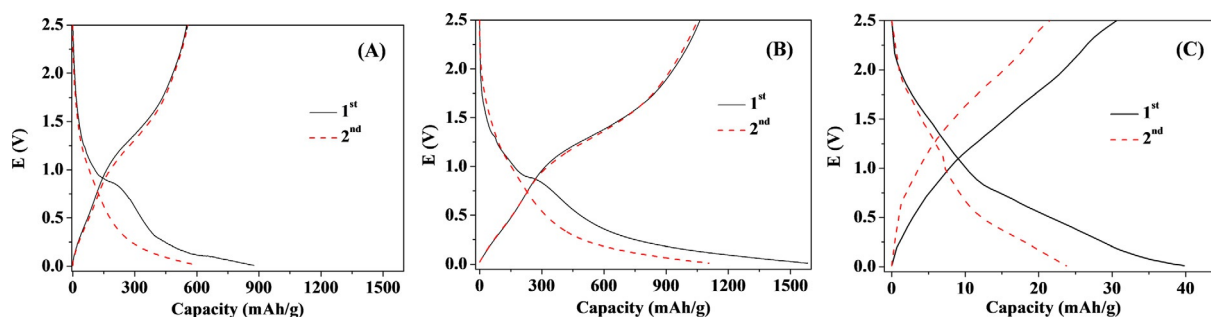**Figure 7.** Galvanostatic charge/discharge curves for the 1st and 2nd cycles of m-WO_3 (A), PANI/m-WO_3 (B), and plain PANI (C) at a current density of 60 mA g^{-1}.

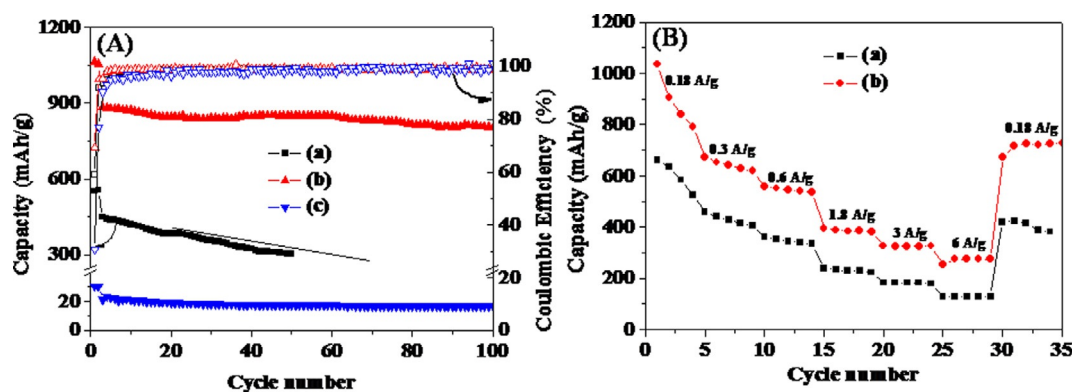**Figure 8.** (A) Cycling performance of m-WO_3 (a), PANI/m-WO_3 (b) and plain PANI (c); (B) Rate capability of m-WO_3 (a) and PANI/m-WO_3 (b) at different current densities.

versible capacities after each five cycles are 523, 406, 334, 223, 178, and 128 mAh g^{-1} for m-WO$_3$ electrode and 792, 618, 536, 383, 327, and 274 mAh g^{-1} for PANI/WO$_3$ electrode, respectively. And for the PANI/m-WO$_3$ electrode, a good capacity recovery of 725 mAh g^{-1} and cycling stability were observed when the current density returned back to 0.18 A g^{-1}, demonstrating the decent high-rate performance of the PANI/m-WO$_3$ electrode. The improvement can be ascribed to the PANI coating layer acting as a conductive binder to increase the contact between the particles, which is similar to the other conducting polymer coating works,[13,31] thus benefitting the Li$^+$ transfer between the m-WO$_3$ matrix and the electrolyte.
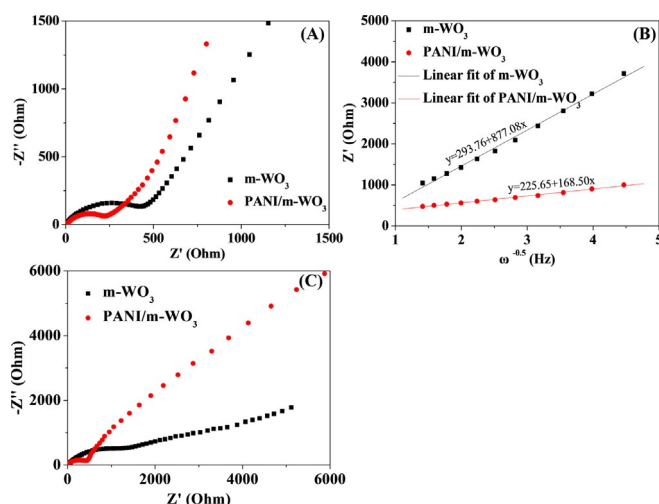
The m-WO$_3$ and PANI/m-WO$_3$ cells after 50 cycles were disassembled in the glovebox and the electrodes were washed with anhydrous dimethyl carbonate three times to remove residual LiPF$_6$ salt and solvents, and then evacuated overnight at room temperature. The as-pretreated electrodes were observed by SEM and EDS, the obtained results are presented in Figure 9. It can be noted that the mesoporosity of the sample disappeared and the particles aggregated for the m-WO$_3$ cell after cycling (Figure 9(A)). This indicates that the volume expansion and aggregation of the particles occurs and the mesoporous structure of the WO$_3$ is broken, which is responsible for the deteriorated cycling stability of the m-WO$_3$ cell. When coated

with PANI, the WO$_3$ particles display a fluffy morphology consisting of nanoparticles, as shown in Figure 9(B), which is inherited from the structure of the fresh PANI/m-WO$_3$. This observation suggests that the polymer coating layer can protect WO$_3$ particles from the expansion and aggregation. The protection of the coating layer can be further confirmed by observing the appearances of the cycled lithium electrodes. As shown in Figure 9(C) and (D), it is obviously that there exist much more deposits on the lithium electrode of the m-WO$_3$ cell than that of the PANI/m-WO$_3$ cell. The EDS detection (Figure 9(E) and (F)) shows that the deposits on the lithium electrode contain C, O, F, and P, which is mainly from the decomposition of the solvents and the LiPF$_6$ salt on m-WO$_3$, and the decomposition products penetrated the separator then transferred to the lithium side. This result suggests that there is serious electrolyte decomposition on the m-WO$_3$ when the cell was cycled over the long term, and this irreversible reaction on the interface of the electrode can be reduced by coating a PANI layer, resulting in improving the electrochemical behavior of the cell.

In order to gain further insight into electrochemical performances of the synthesized samples, the electrochemical impedance spectra of the m-WO$_3$ and PANI/m-WO$_3$ after 5 cycles were measured. As shown in Figure 10(A), both spectra are
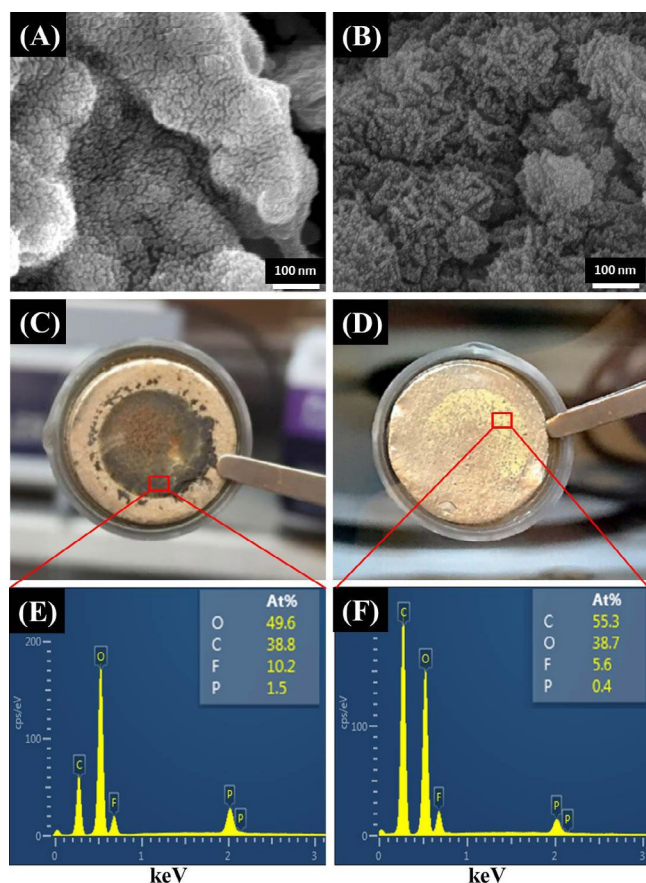
Figure 9. SEM images of m-WO$_3$ (A) and PANI/m-WO$_3$ (B) after 50 cycles; photographs of lithium electrodes disassembled from m-WO$_3$ cell (C) and PANI/m-WO$_3$ cell (D) after 50 cycles; EDS patterns of the surface of the lithium electrodes from cycled m-WO$_3$ cells (E) and PANI/m-WO$_3$ cells (F).

Figure 10. Nyquist plots of the EIS after 5 cycles for m-WO$_3$ and PANI/m-WO$_3$ (A); relationship between Z' and $\omega^{-0.5}$ in the low frequency region (B); Nyquist plots of the EIS after 50 cycles for m-WO$_3$ and PANI/m-WO$_3$ (C).

similar in shape, with a semicircle in the high-frequency region and a sloping line in the low-frequency region. The semicircle is related to the combined processes of surface film (R_{SEI}) and charge transfer resistance (R_{ct}), while the sloping line is attributed to the Warburg impedance, reflecting the Li$^+$ diffusion into the bulk of the electrode material.[32] After coating with PANI, the diameter of the semicircle is markedly smaller than that of pure m-WO$_3$, as shown in Table 1. This result indicates that the presence of PANI improves the charge transfer kinetics, which can be a reason for the higher rate capacity and better cycling performance. Compared to the impedance spec-

Table 1. Pore structure parameters of the samples calculated from the N_2 sorption isotherms and EIS results of m-WO$_3$ and PANI/m-WO$_3$ after 5 cycles.

Sample	Surface area [m^2 g^{-1}]	Pore volume [cm^3 g^{-1}]	Pore size [nm]	Resistance [Ω]	Diffusion coefficients [cm^2 s^{-1}]
m-WO$_3$	106	0.302	13.3	526	1.48×10^{-10}
PANI/ WO$_3$	109	0.270	13.1	244	9.33×10^{-10}
PANI	208	0.484	3.7	–	–

trum of the cell after 5 cycles, the impedance of m-WO$_3$ after 50 cycles increased significantly and displays much higher impedance than that of PANI/m-WO$_3$, as shown in Figure 10 (C). Apparently, the PANI coating layer inhibits the deterioration of the m-WO$_3$ during the cycling, as well as increases the interfacial stability of electrode and electrolyte.

Additionally, the diffusion coefficient (D_{Li}) for the electrodes after 5 cycles can be derived from the plots in the low-frequency region with the following Equations:[33]

$$Z' = R_e + R_{SEI} + R_{ct} + \sigma\omega^{-0.5} \tag{4}$$

$$D_{Li} = \frac{(RT)^2}{2(An^2F^2C_{Li}\sigma)^2} \tag{5}$$

where R_e is uncompensated ohmic resistance between the electrodes, σ is the Warburg factor, ω is the angular frequency, R is the gas constant, T is the absolute temperature, A is the surface area, n is the number of electrons per molecule oxidized, F is the Faraday constant, and C_{Li} is the lithium ion concentration in the bulk material. According to the fitting linear equation in Figure 10 (B) and specific surface area of m-WO$_3$ and PANI/m-WO$_3$ from BET, the diffusion coefficients of Li$^+$ in the m-WO$_3$ and PANI/m-WO$_3$ were estimated to be 1.48×10^{-10} cm^2 s^{-1} and 9.33×10^{-10} cm^2 s^{-1}, respectively. It is evident that the diffusion coefficient of Li$^+$ is increased by the coating of PANI, indicating PANI coating facilitates the lithium-ion transport.

To better understand the contribution of PANI coating to the improved high capacity of m-WO$_3$, the nitrogen-sorption isotherms of the samples were recorded and are shown in Figure 11; the related surface area, pore volumes and pore sizes of samples are summarized in Table 1. The prepared WO$_3$ yields a type IV isotherm with an H1-type hysteresis loop, which is characteristic of cylindrical mesoporous channels. This indicates that the mesostructure of WO$_3$ has been successful replicated from the mesoporous silica template. After loading with PANI, the nitrogen-sorption isotherm of the composite was similar to that of the m-WO$_3$, suggesting that the sample maintained the character of the mesoporous structure. It can be noted that the pore size distribution becomes wider when PANI is loaded, though the pore diameter peak position of the PANI/m-WO$_3$ is similar to the m-WO$_3$ (Figure 11 (B)). As shown in Table 1, the surface area of plain PANI is much higher than that of m-WO$_3$, which indicates that the coating layer itself is porous with the pores on the meso- or nanoscale, resulting in a higher surface area in the PANI/m-WO$_3$ sample compared to the pure m-WO$_3$. The higher surface area in PANI/m-WO$_3$ benefits the penetration of Li$^+$ from the bulk electrolyte to the active electrode materials. However, the pore volumes and BJH pore size are reduced for the composite. This is mainly due to the loading and confinement of PANI within the pore channels of m-WO$_3$ structure, leading to the ordering deterioration of the mesoporous structure of the m-WO$_3$.

From the electrochemical measurements, we can see that the as-prepared PANI/m-WO$_3$ shows larger reversible capacity, better rate capability and cycling stability, and higher coulombic efficiency than the bare m-WO$_3$. The improvement is attributed to the presence of the conducting and flexible polymer polyaniline which improved the electronic conductivity of the composite particles and prevented the detrimental volume expansion of m-WO$_3$ during the lithiation and de-lithiation process. In addition, the chemical interaction between PANI and m-WO$_3$ particles is believed to play an important role in enhancing the electrochemical performance.

Observed from the result of BET, the capacity contribution of the PANI in PANI/m-WO$_3$ can be evaluated by the specific sur-
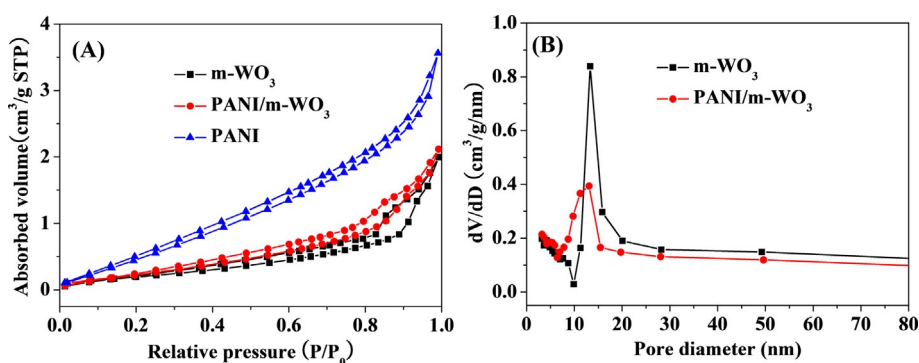
Figure 11. (A) N_2 isotherm adsorption–desorption curves for m-WO$_3$, PANI/m-WO$_3$ and PANI; (B) corresponding pore size distributions for mesostructured m-WO$_3$ and PANI/m-WO$_3$. The pore sizes were analyzed with the adsorption branch using the BJH algorithm.

face area (a_1) of PANI/m-WO$_3$ and the capacity (C_{PANI}) of plain PANI electrode. The PANI matrix was compressed tightly in the plain PANI electrode, thus the intercalation/deintercalation of Li$^+$ was taking place on the surface of the electrode. Therefore, the obtained capacity of plain PANI from the charge/discharge measurement can be changed to specific area capacity (mAh m^{-2}) by the surface area of plain PANI electrode (a_2) from BET result. On the other hand, it is assumed that the m-WO$_3$ particles were completely covered with PANI in PANI/m-WO$_3$ and the specific surface area of PANI/m-WO$_3$ is the value from BET measurement, which means that the intercalation/deintercalation reaction was occurring on a large surface area. Therefore, the ideal contribution capacity (C_i) of plain PANI to PANI/m-WO$_3$ can be calculated by the following Equation (6).

$$C_i \, (\mathrm{mAh\,g^{-1}}) = \frac{C_{PANI}}{a_2} a_1 \qquad (6)$$

The surface area of plain PANI electrode (a_2) is 7.1 m^2 g^{-1} according to the BET result. The resulting C_i is 460 mAh g^{-1}, which might be the cause for the high capacity of PANI/m-WO$_3$. There is no readily available explanation for such a high capacity at the moment, though some possible mechanisms have been considered for future study. The coating of PANI on the surface of m-WO$_3$ may have introduced some synergistic effect for the lithium-ion storage such as a catalyst to promote the reaction at the interface. The introduction of PANI coating may have also retarded the crystal growth during the charge/discharge cycles through promoting heterogeneous high-density nucleation. The fast reaction and high density nucleation may retard the crystallization, retaining the electrode in high energy state and benefitting the charge/discharge process. All the above hypothetical explanations are the subject of our further research.

Conclusions

The polyaniline (PANI)/mesoporous-tungsten trioxide anode nanocomposites prepared through in situ polymerization demonstrated a very high lithium-ion storage capacity with excellent cycling stability after a few initial cycles at a low rate. The PANI layer was evenly coated onto tungsten trioxide particles and the composite shows much higher reversible capacity and better cycling performance than uncoated tungsten trioxide. Such an improvement was attributed to the flexible conductive PANI, and the possible catalytic interaction between PANI and tungsten trioxide particles. In addition, the PANI coating may have promoted fast and high density nucleation and retarded crystallization during the charge and discharge cycles.

Experimental Section

Materials synthesis

Mesoporous WO$_3$: Mesoporous silica KIT-6 template was prepared according to a previously reported procedure.[28] Ordered mesoporous WO$_3$ was prepared as follows. 2.4 g of 12-phosphotungstic acid was dissolved into 40 mL of ethanol, which was then mixed with 1.6 g of KIT-6 template under stirring. After evaporation of the ethanol at 60 °C, the obtained white powders were calcined at 500 °C for 3 h to give a decomposition product of tungsten trioxide. The KIT-6 template was then removed with 2 M hydrogen fluoride solution under constant magnetic stirring for overnight at room temperature.[20]

PANI/m-WO$_3$: 0.4 g of as-prepared m-WO$_3$ powder was dispersed in ultrasonically in 40 mL of 0.1 M hydrochloric acid. 80 mg aniline monomer was added to the mixture under constant magnetic stirring in the ice bath. 89.6 mg ammonium peroxydisulfate was added in 20 mL 0.1 M hydrochloric acid solution and precooled to 0 °C, then added slowly to the mixture under constant magnetic stirring in the ice bath. After polymerization for 6 h in the ice bath, dark green powder was collected by filtration and rinsed with water and methanol and dried at 60 °C under vacuum. The plain PANI was prepared by the same method without m-WO$_3$ and deep dark green powder was obtained after the washing and drying process.

Materials characterization

The crystal structure of the composite was determined by XRD (D8 Bruker X-ray diffractometer with Cu$_{K\alpha}$ radiation ($\lambda = 1.5418$ Å)) within the range of 10°–80° (2θ). FTIR were carried out on a BRUKER TENSOR27 spectrophotometer within 400–4000 cm^{-1} using an attenuated total reflection mode. The energy dispersive X-ray spectroscopy (EDS) and the morphology were observed with SEM (JEOL, JSM-7000F) and TEM (JEM-2100 h) operating at 200 kV. TGA was performed on a TG instrument (NET ZSCH STA 409C). The specific surface area and micropore and mesopore volumes were determined by multipoint Brunauer–Emmett–Teller (BET), t-method, and Barret–Joyner–Halenda (BJH) desorption analyses, respectively.

Electrochemical measurements

The electrodes of m-WO$_3$, PANI/m-WO$_3$, and plain PANI were prepared by coating a mixture of 70 wt.% of active material and 15 wt.% of super-p as conducting agent and 15 wt.% of sodium carboxymethyl-cellulose as binder onto a Cu current collector. The electrodes were pressed to 10 MPa for 5 min to compress the electrode materials matrix tightly before the coin cells assembly. 2016-type coin cells were assembled in an Ar-filled MBraun glove box using the prepared electrodes as working electrodes, lithium foils as counter electrodes and microporous membrane (Celgard 2400) as the separators. The base electrolyte in this work was 1.0 mol dm^{-3} LiPF$_6$ in ethylene carbonate (EC)/ethyl methyl carbonate (EMC)/diethyl carbonate (DEC) (1:1:1).

Cycling voltammetry was performed on Solartron-1470 instrument (England) with m-WO$_3$ and PANI/m-WO$_3$ electrode as working electrode and lithium as reference and counter electrode at 25 °C at a sweep rate of 0.1 mV s^{-1}. For better comparisons of the CV results, the same loading weights of the anode materials were selected. The charge–discharge tests were conducted on a LAND cell test system (Land CT 2001A) and cycled between 2.5 and 0.01 V (vs. Li$^+$/Li) at 25 °C. The capacity of the m-WO$_3$ and PANI/m-WO$_3$ were calculated on the basis of WO$_3$. Electrochemical impedance spectroscopies (EIS) were performed on the Solartron 1287A in conjunction with a Solartron 1260FRA/impedance analyzer with amplitude of 10.0 mV in the frequency range from 100 kHz to 0.1 Hz. Before the EIS measurement, the electrodes were charged to 1.5 V (vs. Li$^+$/Li) and kept at this potential for 2 h to reach an identical status.

Acknowledgements

Keywords: lithium-ion batteries · mesoporous materials · polyaniline · tungsten trioxide

[1] a) K. Xu, *Chem. Rev.* **2014**, *114*, 11503 – 11618; b) E. Uchaker, G. Cao, *Nano Today* **2014**, *9*, 499 – 524; c) Q. F. Zhang, S. L. Candelaria, E. Uchaker, G. Z. Cao, *Chem. Soc. Rev.* **2013**, *42*, 3127 – 3171; d) R. C. Massé, E. Uchaker, G. Cao, *Sci. China Mater.* **2015**, *58*, 715 – 766; e) J. Yue, C. Suchomski, T. Brezesinski, B. M. Smarsly, *ChemNanoMat* **2015**, *1*, 415 – 421.

[2] C. Guo, L. Wang, Y. Zhu, D. Wang, Qi. Yang, Y. Qian, *Nanoscale* **2015**, *7*, 10123 – 10129.

[3] a) L. Tian, Q. Zhuang, J. Li, C. Wu, Y. Shi, S. Sun, *Electrochim. Acta* **2012**, *65*, 153 – 158; b) C. Wu, X. Li, W. Li, B. Li, Y. Wang, Y. Wang, M. Xu, L. Xing, *J. Power Sources* **2014**, *251*, 85 – 91.

[4] D. Ge, H. Geng, J. Wang, J. Zheng, Y. Pan, X. Cao, H. Gu, *Nanoscale* **2014**, *6*, 9689 – 9694.

[5] a) M. Zhang, Y. Li, E. Uchaker, S. Candelaria, L. Shen, T. Wang, G. Cao, *Nano Energy* **2013**, *2*, 769 – 778; b) N. Zhao, G. Wang, Y. Huang, B. Wang, B. Yao, Y. Wu, *Chem. Mater.* **2008**, *20*, 2612 – 2614.

[6] a) Z. X. Huang, Y. Wang, Y. G. Zhu, Y. Shi, J. I. Wong, H. Y. Yang, *Nanoscale* **2014**, *6*, 9839 – 9845; b) Q. Gao, L. Yang, X. Lu, J. Mao, Y. Zhang, Y. Wu, Y. Tang, *J. Mater. Chem.* **2010**, *20*, 2807 – 2812.

[7] a) Z. Hong, M. Wei, T. Lan, G. Cao, *Nano Energy* **2012**, *1*, 466 – 471; b) J. Lei, W. Li, X. Li, E. J. Cairns, *J. Mater. Chem.* **2012**, *22*, 22022 – 22027.

[8] H. B. Lin, H. B. Rong, W. Z. Huang, Y. H. Liao, L. D. Xing, M. Q. Xu, X. P. Li, W. S. Li, *J. Mater. Chem. A* **2014**, *2*, 14189 – 14194.

[9] S. Yoon, C. Jo, S. Y. Noh, C. W. Lee, J. H. Song, J. Lee, *Phys. Chem. Chem. Phys.* **2011**, *13*, 11060 – 11066.

[10] L. Gao, X. Wang, Z. Xie, W. Song, L. Wang, X. Wu, F. Qu, D. Chen, G. Shen, *J. Mater. Chem. A* **2013**, *1*, 7167 – 7173.

[11] M. Sasidharan, N. Gunawardhana, M. Yoshio, K. Nakashima, *Nano Energy* **2012**, *1*, 503 – 508.

[12] F. Liu, J. G. Kim, C. W. Lee, J. S. Im, *Appl. Surf. Sci.* **2014**, *316*, 604 – 609.

[13] W. Tang, L. Liu, Y. Zhu, H. Sun, Y. Wu, K. Zhu, *Energy Environ. Sci.* **2012**, *5*, 6909 – 6913.

[14] a) Z. Yin, Q. Zheng, *Adv. Energy Mater.* **2012**, *2*, 179 – 218; b) J. H. Cheung, W. B. Stockton, M. F. Rubner, *Macromolecules* **1997**, *30*, 2712 – 2716; c) X. Li, M. Rao, H. Lin, D. Chen, Y. Liu, S. Liu, Y. Liao, L. Xing, M. Xu, W. Li, *J. Mater. Chem. A* **2015**, *3*, 18098 – 18104.

[15] J.-M. Jeong, B. G. Choi, S. C. Lee, K. G. Lee, S.-J. Chang, Y.-K. Han, Y. B. Lee, H. U. Lee, S. Kwon, G. Lee, C.-S. Lee, Y. S. Huh, *Adv. Mater.* **2013**, *25*, 6250 – 6255.

[16] M. Kummer, J. P. Badillo, A. Schmitz, H.-G. Bremes, M. Winter, C. Schulz, H. Wiggers, *J. Electrochem. Soc.* **2014**, *161*, A40 – A45.

[17] D. Ge, L. Yang, A. Honglawan, J. Li, S. Yang, *Chem. Mater.* **2014**, *26*, 1678 – 1685.

[18] Y. Wang, B. Li, L. Zeng, D. Cui, X. Xiang, W. Li, *Biosens. Bioelectron.* **2013**, *41*, 582 – 588.

[19] F. Kleitz, S. H. Choi, R. Ryoo, *Chem. Commun.* **2003**, 2136 – 2137.

[20] X. Cui, J. Shi, H. Chen, L. Zhang, L. Guo, J. Gao, J. Li, *J. Phys. Chem. B* **2008**, *112*, 12024 – 12031.

[21] S. Bhadra, S. Chattopadhyay, N. K. Singha, D. Khastgir, *J. Appl. Polym. Sci.* **2008**, *108*, 57 – 64.

[22] A. Malinauskas, J. Malinauskiene, A. Ramanavičius, *Nanotechnology* **2005**, *16*, R51 – R62.

[23] H. Wei, X. Yan, S. Wu, Z. Luo, S. Wei, Z. Guo, *J. Phys. Chem. C* **2012**, *116*, 25052 – 25064.

[24] R. M. Khafagy, *J. Alloys Compd.* **2011**, *509*, 9849 – 9857.

[25] a) K. Mohanraju, V. Sreejith, R. Ananth, L. Cindrella, *J. Power Sources* **2015**, *284*, 383 – 391; b) J. Shi, H. Xu, H. Zhao, L. Lu, *J. Power Sources* **2012**, *205*, 129 – 135.

[26] S. Yoon, S.-G. Woo, K.-N. Jung, H. Song, *J. Alloys Compd.* **2014**, *613*, 187 – 192.

[27] Y. Qiu, G.-L. Xu, Q. Kuang, S.-G. Sun, S. Yang, *Nano Res.* **2012**, *5*, 826 – 832.

[28] a) X. Cao, X. Chuan, R. C. Massé, D. Huang, S. Li, G. Cao, *J. Mater. Chem. A* **2015**, *3*, 22739 – 22749; b) M. Zhang, T. H. Wang, G. Z. Cao, *Int. Mater. Rev.* **2015**, *60*, 330 – 352.

[29] W. X. Chen, Z. Xu, L. S. Yang, *J. Power Sources* **2001**, *102*, 112 – 117.

[30] B.-X. Zou, Y. Liang, X.-X. Liu, D. Diamond, K.-T. Lau, *J. Power Sources* **2011**, *196*, 4842 – 4848.

[31] a) W. Tang, X. Gao, Y. Zhu, Y. Yue, Y. Shi, Y. Wu, K. Zhu, *J. Mater. Chem.* **2012**, *22*, 20143 – 20145; b) Y. Liu, B. H. Zhang, S. Y. Xiao, L. L. Liu, Z. B. Wen, Y. P. Wu, *Electrochim. Acta* **2014**, *116*, 512 – 517.

[32] a) S. Hu, F. Yin, E. Uchaker, W. Chen, M. Zhang, J. Zhou, Y. Qi, G. Cao, *J. Phys. Chem. C* **2014**, *118*, 24890 – 24897; b) B. Z. Li, Y. Wang, L. Xue, X. P. Li, W. S. Li, *J. Power Sources* **2013**, *232*, 12 – 16.

[33] a) Q. Cao, H. P. Zhang, G. J. Wang, Q. Xia, Y. P. Wu, H. Q. Wu, *Electrochem. Commun.* **2007**, *9*, 1228 – 1232; b) H. Song, Y. Liu, C. Zhang, C. Liu, G. Cao, *J. Mater. Chem. A* **2015**, *3*, 3547 – 3558; c) X. Xiang, W. Li, *Electrochim. Acta* **2014**, *127*, 259 – 265.